

Continuous-Time Ultra-Wideband-Inertial Fusion

Kailai Li, Ziyu Cao, and Uwe D. Hanebeck

Abstract—We present a novel continuous-time online state estimation framework using ultra-wideband and inertial sensors. For representing motion states continuously over time, quaternion-based cubic B-splines are exploited with efficient solutions to kinematic interpolations and spatial differentiations. Based thereon, a sliding-window spline fitting scheme is established for asynchronous multi-sensor fusion and online calibration. We evaluate the proposed system, SFUISE (spline fusion-based ultra-wideband-inertial state estimation), in real-world scenarios based on public data set and experiments. The proposed spline fusion scheme is real-time capable and delivers superior performance over state-of-the-art discrete-time schemes. We release the source code and own experimental data set at <https://github.com/KIT-ISAS/SFUISE>.

Index Terms—Sensor fusion, localization.

I. INTRODUCTION

Online estimation of dynamical motions is of fundamental importance in achieving reliable autonomy of mobile robots [1]–[5]. Recent development in ultra-wideband (UWB) technology has provided promising alternative solutions to localization in GPS-denied environments. Compared with common sensing principles, e.g., cameras or LiDARs, UWB sensors are lightweight, low-cost and more scalable for large-scale deployment, in particular, in indoor scenarios [6].

While impulse radio of UWBs transmits at nano-second level and reaches very high spatial resolutions, there still exist technical difficulties towards high-performance UWB-based tracking in practice. Well-known issues for UWB ranging include non-line-of-sight (NLOS) and multipath conditions, which may even escalate due to complex and time-varying surroundings (e.g., with moving objects) [7]. Desired line-of-sight (LOS) measurements, on the other hand, often exhibit scenario-dependent and untypical noise patterns [8]. Moreover, interference and diffraction of radio signals vary among objects of different materials and are impossible to model. Thus, UWB-only tracking based on multilateration is almost always insufficient to estimate highly dynamical motions and can deliver springy trajectories that are physically infeasible.

This work is partially supported by the German Federal Ministry of Education and Research (BMBF) under grant POMAS (FKZ 01IS17042) and German Research Foundation (DFG) under grant HA 3789/25-1. (Corresponding author: Kailai Li.)

Kailai Li is with the Department of Electrical Engineering, Linköping University, Linköping, Sweden. The work was done with Ziyu Cao and Uwe D. Hanebeck at the Intelligent Sensor-Actuator-Systems Laboratory (ISAS), Institute for Anthropomatics and Robotics, Karlsruhe Institute of Technology (KIT), Karlsruhe, Germany. E-mails: kailai.li@liu.se, ziyu.cao@kit.edu, uwe.hanebeck@kit.edu.

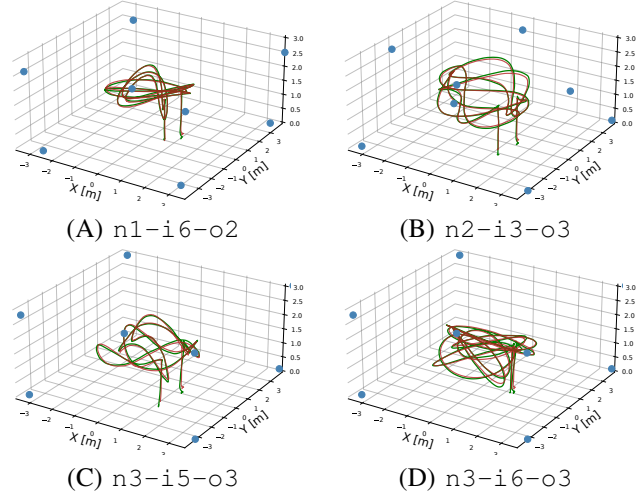


Fig. 1: Exemplary runs of SFUISE on UTIL data set.

In order to improve the performance of UWB-based tracking, one common solution is to fuse other sensory modalities with UWB ranging. Inertial sensors provide instant and higher-order motion information that can bridge the gap between consecutive UWB readings. Compared with other typical sensors for state estimation, they are cost- and resource-efficient and straightforward to deploy to UWB sensor networks. Conventional UWB-inertial fusions adopt recursive filtering algorithms, in particular, the extended Kalman filter (EKF) among others, with inertial measurements facilitating state propagation and ultra-wideband ranging updating the predicted prior. One basic application was introduced in [9], where an EKF was deployed to localizing micro aerial vehicles using UWB-inertial setup. Further practices include six-DoF motion estimation based on quaternion kinematics [7] and incorporating error-states for performance improvement [10], [11].

However, recursive filters rely on the Markov chain assumption, where evidence for predicting current state is only traced back to the last state [5]. Sensor measurements of different modalities are usually fused in a decoupled manner, inducing substantial information loss in correlations across multi-sensor readings [3]. These issues can be substantially mitigated by fusing sensor measurements into one joint graph-based nonlinear optimization. It improves tracking accuracy, while still maintaining tractable computational complexity thanks to its sparse structure [12]. Such a paradigm shift has been predominantly reflected in visual- or LiDAR-based odometry [2], [13], [14]. For UWB-inertial state estimation, related techniques are yet fully updated with

state-of-the-art methodology. Most use cases are limited to batchwise (offline) [15] or planar motion estimation [6].

More importantly, both filtering and graph-based fusion schemes are built atop discrete timestamps of constant interval, where incorporating kinematic constraints and temporal continuity in state transitions is inherently prohibited. From an engineering perspective, different sensors fire in principle asynchronously without any common time instant. Even under a single-sensor setup, measurements can be nonuniformly sampled over time due to timestamp jitter (especially in ultra-wideband sensing) [7]. Moreover, discrete-time sensor fusion often refers to measurement interpolation w.r.t. timestamps of estimates, inducing extra approximation error. Performance of UWB-based tracking, in particular, can easily deteriorate due to interpolating asynchronous range measurements from different anchors under outliers and complex noise patterns.

Recent advance in applying B-splines to motion representation has enlightened promising direction for continuous-time sensor fusion. Instead of modeling states at discrete timestamps, B-splines parameterize trajectories atop control points through temporal polynomials, enabling interpolation at any given time instant with locality and smoothness. This concept can be practically generalized to Lie groups or non-linear manifolds via reformulation into a cumulative form, based on which rigid body motions can be modeled continuously over time. In [16], [17], B-splines were first applied to estimating continuous-time states via batchwise maximum a posteriori. Similar offline schemes were further proposed for attitude estimation [18], multi-sensor calibration [19], and trajectory estimation with visual/event-inertial or LiDAR-inertial setups [20]–[23]. However, these batchwise schemes are computationally expensive, as computing time derivatives and Jacobians on B-splines for optimization typically rely on numerical or automatic differentiations.

One breakthrough towards online continuous-time motion estimation using B-splines was made in [24], where efficient solutions to computing time derivatives and Jacobians on $SO(3)$ trajectories were introduced to spline fitting. This has quickly inspired a series of successive work in online motion estimation with applications such as RGB-D tracking, visual-inertial calibration and odometry [25]–[28].

Though progress in spline-based state estimation has been ongoing, there still remains considerable gap towards more extensive engineering practice. To the best knowledge of the authors, there exists by far no continuous-time solution to UWB-inertial fusion. Moreover, existing online B-spline fitting schemes depend heavily on the theory and implementation in [24] based on matrix Lie group $SO(3)$. However, unit quaternions are preferable for representing rotations in most robotic applications, and no B-spline fusion scheme has been systematically established based thereon for online multi-sensor fusion (in particular involving IMUs).

Contribution

In light of state of the art, we propose a novel spline fusion scheme for continuous-time UWB-inertial state estimation (Sec. II). Quaternion-based cubic cumulative B-splines are

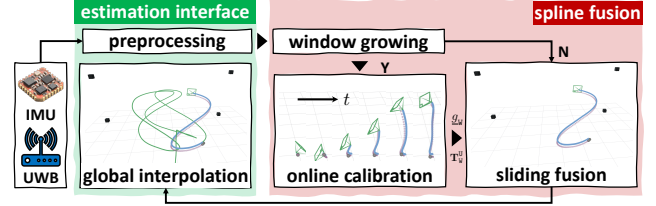


Fig. 2: System pipeline.

applied as backbone to state representation, for which closed-form kinematic interpolations and Jacobians are derived for efficient spline fitting (Sec. III). Based thereon, a sliding-window fusion scheme is established for fusing UWB-inertial readings at raw timestamps with online calibration (Sec. IV). We evaluate our system in various real-world scenarios based on experiments and public data sets, including comparisons with state-of-the-art discrete-time fusion schemes (Sec. V). The proposed scheme delivers real-time and superior performance over the discrete-time counterparts. Considering the generality of the proposed scheme to extensive scenarios, we open-source our implementation together with own experimental data sets.

II. SYSTEM OVERVIEW

In the considered scenario, we aim to estimate the following motion-related states

$$\underline{x}(t) = [\underline{r}(t)^\top, \underline{s}(t)^\top, \underline{b}(t)^\top]^\top \in \mathbb{S}^3 \times \mathbb{R}^3 \times \mathbb{R}^6 \subset \mathbb{R}^{13} \quad (1)$$

as a function over time. Quaternion $\underline{r}(t) \in \mathbb{S}^3$ and vector $\underline{s}(t) \in \mathbb{R}^3$ denote orientations and positions, respectively, and $\underline{b}(t) = [\underline{b}_{acc}^\top, \underline{b}_{gyro}^\top]^\top \in \mathbb{R}^6$ incorporates biases of accelerometer and gyroscope. As shown in Fig. 2, the proposed continuous-time tracking system is composed of an estimation interface and a functional core of spline fusion. Asynchronous UWB and IMU measurements of different rates are first preprocessed for downsampling, to which a cubic B-spline is then fitted over a time window of limited span. As sensor data are streamed in, the spline fusion window first grows to a pre-given width, afterward slides, both w.r.t. the current timestamp for online state estimation. In the growing stage, additional online calibrations are performed to obtain the gravity vector \underline{g}^w and transformation $\mathbf{T}_w^U \in SE(3)$ from world to UWB frames. Further, control point estimates given by spline fusion are sent back to estimation interface, where a global spline is maintained and interpolated to obtain trajectory estimates. We now detail the backend spline fusion module in the upcoming sections.

III. STATE ESTIMATION ON CUMULATIVE B-SPLINES

A. Continuous-Time State Modeling

We deploy cubic (fourth-order) cumulative B-splines for continuous-time state representation. Being established upon a set of *control points* $\{(\underline{d}_i, t_i)\}_{i=1}^n$ associated with time t_i of uniform interval, it allows for fusing sensor readings up to the second order of motion (e.g., from accelerometer) [24]. State

at an arbitrary timestamp $t \in [t_i, t_{i+1})$ can be interpolated w.r.t. a local set of control points $\{\underline{d}_{i+j-2}\}_{j=0}^3$ according to

$$\underline{s}(t) = \underline{d}_{i-2} + \sum_{j=1}^3 \lambda_j(u) \underline{\delta}_j, \quad \text{with } u = \frac{t - t_i}{t_{i+1} - t_i} \quad (2)$$

being the normalized time and $\underline{\delta}_j = \underline{d}_{i+j-2} - \underline{d}_{i+j-3}$ the distance between neighboring control points. The cumulative basis functions $\{\lambda_j(u)\}_{j=1}^3$ are given by $\underline{\lambda}(u) = [\lambda_1(u), \lambda_2(u), \lambda_3(u)]^\top = \Phi \underline{u}$, with

$$\Phi = \frac{1}{6} \begin{bmatrix} 5 & 3 & -3 & 1 \\ 1 & 3 & 3 & -2 \\ 0 & 0 & 0 & 1 \end{bmatrix} \quad \text{and } \underline{u} = [1, u, u^2, u^3]^\top,$$

which endows cubic B-splines with C^2 -continuity. The concept of B-splines can be naturally extended to the manifold of unit quaternions based on Riemannian geometry. It follows

$$\underline{r}(t) = \underline{r}_{i-2} \otimes \prod_{j=1}^3 \text{Exp}_{\mathbb{H}}(\lambda_j(u) \underline{\delta}_j), \quad (3)$$

with \otimes denoting the Hamilton product and $\lambda_j(u)$ the basis functions in (2). Distance between adjacent control points is quantified via logarithm map $\underline{\delta}_j = \text{Log}_{\mathbb{H}}(\underline{r}_{i+j-3}^{-1} \otimes \underline{r}_{i+j-2})$ at identity $\mathbb{1} = [1, 0, 0, 0]^\top$ and contributes to on-manifold interpolation via exponential map $\text{Exp}_{\mathbb{H}}(\cdot)$ [29].

On modeling motion-related states, control points are optimally estimated by fitting the spline to measurements in the sense of least squares. Constructing residuals in the objective refers to kinematic interpolations on cubic B-splines w.r.t. related sensory modalities. This can be computationally expensive due to large data volume and complexity in deriving motion derivatives. Meanwhile, solving the nonlinear least squares requires Jacobians of on-manifold kinematic interpolations w.r.t. control points. Due to theoretical difficulty, most existing systems rely on numerical or automatic differentiations [18], [20], [21], with only a few online schemes of choices with efficient analytical solutions based on matrix Lie groups [24], [25]. For quaternion-based B-splines, no systematic and open-source work exists regarding analytical kinematic interpolations and gradients w.r.t. control points. In the remainder of this section, we provide these fundamental theoretical building blocks towards high-performance online spline fusion.

B. Kinematic Interpolations

In consideration of common kinematic measurements, we now provide time derivatives of cubic B-splines to interpolate linear velocity and acceleration, and angular velocity.

Linear velocity and acceleration: Given a position B-spline $\underline{s}(t)$ in (2), its first-order time derivative (denoted by dot atop the variable) can be derived via $\dot{\underline{s}}(t) = \underline{s}'(u)u'(t)$, with $u'(t) = 1/(t_{i+1} - t_i) := 1/\Delta_i$. This leads to

$$\dot{\underline{s}}(t) = \sum_{j=1}^3 \lambda_j'(u) \underline{\delta}_j u'(t) = \sum_{j=1}^3 \dot{\lambda}_j(u) \underline{\delta}_j,$$

with $\dot{\lambda}_j$ being derivatives of basis functions in (2) given by $[\dot{\lambda}_1(u), \dot{\lambda}_2(u), \dot{\lambda}_3(u)]^\top = \Phi [0, 1, 2u, 3u^2]^\top / \Delta_i$. Further, the acceleration over time follows

$$\ddot{\underline{s}}(t) = \underline{s}''(u)u'(t) = \sum_{j=1}^3 \ddot{\lambda}_j(u) \underline{\delta}_j, \quad (4)$$

with $[\ddot{\lambda}_1(u), \ddot{\lambda}_2(u), \ddot{\lambda}_3(u)]^\top = \Phi [0, 0, 2, 6u]^\top / \Delta_i^2$.

Angular velocity: By definition [10], directly computing the time derivative of the quaternion spline function in (3) leads to the angular velocity $\underline{\omega}(t)$ in body frame via relation

$$\dot{\underline{r}}(t) = 0.5 \underline{r}(t) \otimes \underline{\omega}(t). \quad (5)$$

In practice, however, this requires quadratic complexity w.r.t. spline order due to the chain of Hamilton products. For cumulative B-spline on matrix Lie group $\text{SO}(3)$, an efficient recursive method has been introduced in [18]. We hereby provide the full derivation for its quaternion counterpart.

For brevity, we discard the time variable in (3) and split the product chain into $\underline{r} = \underline{r}_k \otimes \prod_{j=k+1}^3 \text{Exp}_{\mathbb{H}}(\lambda_j \underline{\delta}_j)$, where $\underline{r}_k = \underline{r}_{i-2} \otimes \prod_{j=1}^k \text{Exp}_{\mathbb{H}}(\lambda_j \underline{\delta}_j)$ for $k \in \{1, 2, 3\}$. The quaternion spline interpolation can then be expressed in a recursive fashion according to

$$\underline{r}_k = \underline{r}_{k-1} \otimes \underline{e}_k, \quad (6)$$

with $\underline{e}_k := \text{Exp}_{\mathbb{H}}(\lambda_k \underline{\delta}_k)$ denoting the k -th spline increment obtained from exponential map. Applying the kinematic relation in (5) to \underline{r}_k yields

$$\dot{\underline{r}}_k = 0.5 \underline{r}_k \otimes \underline{\omega}_k, \quad (7)$$

with $\underline{\omega}_k$ being the angular velocity to be computed recursively. For that, we take time derivative of (6) and obtain

$$\dot{\underline{r}}_k = \dot{\underline{r}}_{k-1} \otimes \underline{e}_k + \underline{r}_{k-1} \otimes \dot{\underline{e}}_k, \quad (8)$$

where time derivative of increment \underline{e}_k is given by

$$\dot{\underline{e}}_k = \underline{e}_k \otimes (\dot{\lambda}_k \underline{\delta}_k), \quad (9)$$

according to (5) and quaternion logarithm map in (18). (8) can then be further derived as

$$\begin{aligned} \dot{\underline{r}}_k &= 0.5 \underline{r}_{k-1} \otimes \underline{\omega}_{k-1} \otimes \underline{e}_k + \underline{r}_{k-1} \otimes \underline{e}_k \otimes (\dot{\lambda}_k \underline{\delta}_k) \\ &= 0.5 \underline{r}_k \otimes (\underline{e}_k^{-1} \otimes \underline{\omega}_{k-1} \otimes \underline{e}_k + 2\dot{\lambda}_k \underline{\delta}_k), \end{aligned}$$

based on (6) and (7). Subsequently, following recursive expression for angular velocity interpolation on quaternion cubic B-spline can be established

$$\underline{\omega}_k = \mathcal{R}(\underline{e}_k^{-1}) \underline{\omega}_{k-1} + 2\dot{\lambda}_k \underline{\delta}_k, \quad (10)$$

where $\mathcal{R}(\underline{e}_k^{-1}) \underline{\omega}_{k-1} = \underline{e}_k^{-1} \otimes \underline{\omega}_{k-1} \otimes \underline{e}_k$ rotates angular velocity $\underline{\omega}_{k-1}$ according to the inverse quaternion increment \underline{e}_k^{-1} . In order to bootstrap the recursion, we can derive $\underline{\omega}_1$ via time derivative of $\underline{r}_1 = \underline{r}_{i-2} \otimes \underline{e}_1$ according to (9), namely,

$$\dot{\underline{r}}_1 = \underline{r}_{i-2} \otimes \dot{\underline{e}}_1 = \underline{r}_{i-2} \otimes \underline{e}_1 \otimes (\dot{\lambda}_1 \underline{\delta}_1) = \underline{r}_1 \otimes (\dot{\lambda}_1 \underline{\delta}_1),$$

leading to $\underline{\omega}_1 = 2\dot{\lambda}_1 \underline{\delta}_1$. Alternatively, the recursion can be initialized at zeroth step with vector $\underline{\omega}_0 = \underline{0}_3 \in \mathbb{R}^3$.

C. Spatial Differentiations

The kinematic interpolations on cubic B-splines in Sec. III-B further facilitate constructing residuals given sensor measurements in spline fitting. On computing objective's gradient via the chain rule in nonlinear optimization, the major complexity goes to the kinematic terms. For that, we consider a spline segment ranging over $t \in [t_i, t_{i+1})$ as introduced in

Sec. III-A. Jacobians of interpolated kinematic states \underline{x} w.r.t. control points $\{\underline{x}_{i+j-2}\}_{j=0}^3$ are in principle expressed as

$$d\underline{x}/d\underline{x}_{i+j-2} = \mathbb{I}_{j=0}\mathbf{J}_{i-2} + \mathbb{I}_{j \neq 0}\mathbf{J}_j + \mathbb{I}_{j \neq 3}\mathbf{J}_{j+1}, \quad (11)$$

with \mathbb{I} being the indicator function. Depending on the control point indices, Jacobian components in (11) are calculated via

$$\mathbf{J}_{i-2} = \frac{\partial \underline{x}}{\partial \underline{x}_{i-2}}, \mathbf{J}_j = \frac{\partial \underline{x}}{\partial \underline{\delta}_j} \frac{\partial \underline{\delta}_j}{\partial \underline{x}_{i+j-2}}, \mathbf{J}_{j+1} = \frac{\partial \underline{x}}{\partial \underline{\delta}_{j+1}} \frac{\partial \underline{\delta}_{j+1}}{\partial \underline{x}_{i+j-2}}$$

that are concretized according to kinematic types as follows.

Jacobians of position and orientation interpolations: Following (11), it is trivial to obtain the Jacobian of position spline w.r.t control points as follows

$$\frac{d\underline{s}}{d\underline{\delta}_{i+j-2}} = (\mathbb{I}_{j=0} + \mathbb{I}_{j \neq 0}\lambda_j - \mathbb{I}_{j \neq 3}\lambda_{j+1})\mathbf{I}_3.$$

For the orientation spline defined in (3), its first Jacobian component in (11) is derived as

$$\mathbf{J}_{i-2} = \mathcal{Q}^\perp \left(\prod_{j=1}^3 \underline{e}_j \right),$$

with function \mathcal{Q}^\perp mapping a quaternion multiplied from right-hand side into its matrix representation [29]. In order to obtain the Jacobian components \mathbf{J}_j and \mathbf{J}_{j+1} in (11), we reformulate the quaternion interpolation function (3) into

$$\underline{r} = \left(\underline{r}_{i-2} \otimes \prod_{k=1}^{j-1} \underline{e}_k \right) \otimes \underline{e}_j \otimes \prod_{k=j+1}^3 \underline{e}_k = \mathbf{Q}_\leftarrow^\perp \mathbf{Q}_\rightarrow^\perp \underline{e}_j$$

to expose the j -th increment \underline{e}_j . $\mathbf{Q}_\leftarrow^\perp$ and $\mathbf{Q}_\rightarrow^\perp$ are matrices representing the quaternions multiplied on the left- and right-hand sides of \underline{e}_j via \mathcal{Q}^\perp and \mathcal{Q}^\perp , respectively, i.e.,

$$\mathbf{Q}_\leftarrow^\perp = \mathcal{Q}^\perp \left(\underline{r}_{i-2} \otimes \prod_{k=1}^{j-1} \underline{e}_k \right), \mathbf{Q}_\rightarrow^\perp = \mathcal{Q}^\perp \left(\prod_{k=j+1}^3 \underline{e}_k \right).$$

We then obtain the gradient of quaternion spline w.r.t. $\underline{\delta}_j$ (also valid for $\underline{\delta}_{j+1}$ by changing the index) as

$$\frac{\partial \underline{r}}{\partial \underline{\delta}_j} = \lambda_j \mathbf{Q}_\leftarrow^\perp \mathbf{Q}_\rightarrow^\perp \frac{\partial \text{Exp}_\perp(\underline{v})}{\partial \underline{v}} \bigg|_{\underline{v}=\lambda_j \underline{\delta}_j},$$

with the gradient of exponential map provided in Appendix A. The gradient of $\underline{\delta}_j$ w.r.t. control point follows

$$\frac{\partial \underline{\delta}_j}{\partial \underline{x}_{i+j-2}} = \frac{\partial \text{Log}_\perp(\underline{d}_j)}{\partial \underline{x}_{i+j-2}} = \frac{\partial \text{Log}_\perp(\underline{r})}{\partial \underline{r}} \bigg|_{\underline{r}=\underline{d}_j} \mathcal{Q}^\perp(\underline{x}_{i+j-3}^{-1}), \quad (12)$$

with $\underline{d}_j := \underline{x}_{i+j-3}^{-1} \otimes \underline{x}_{i+j-2}$. We give the gradient of logarithm map in Appendix B, and the gradient of $\underline{\delta}_{j+1}$ is

$$\frac{\partial \underline{\delta}_{j+1}}{\partial \underline{x}_{i+j-2}} = \frac{\partial \text{Log}_\perp(\underline{r})}{\partial \underline{r}} \bigg|_{\underline{r}=\underline{d}_{j+1}} \mathcal{Q}^\perp(\underline{x}_{i+j-1}) \mathbf{D},$$

where $\mathbf{D} = \text{diag}(1, -1, -1, -1)$ denotes a diagonal matrix.

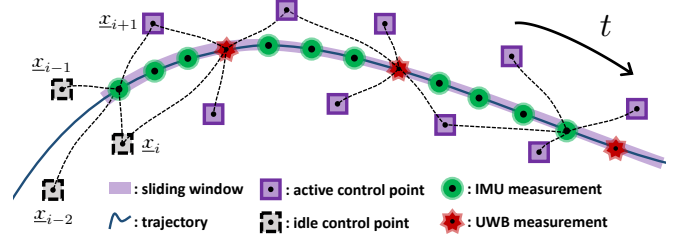


Fig. 3: Sliding-window spline fitting for online estimation.

Jacobian of angular velocity interpolation: In reference to (11), the Jacobian takes the following general form

$$\frac{d\underline{\omega}}{d\underline{x}_{i+j-2}} = \mathbb{I}_{j \neq 0}\underline{\Omega}_j + \mathbb{I}_{j \neq 3}\underline{\Omega}_{j+1}, \quad (13)$$

with the two partial derivatives expressed as follows

$$\underline{\Omega}_j = \frac{\partial \underline{\omega}}{\partial \underline{\omega}_j} \frac{\partial \underline{\omega}_j}{\partial \underline{\delta}_j} \frac{\partial \underline{\delta}_j}{\partial \underline{x}_{i+j-2}}, \underline{\Omega}_{j+1} = \frac{\partial \underline{\omega}}{\partial \underline{\omega}_{j+1}} \frac{\partial \underline{\omega}_{j+1}}{\partial \underline{\delta}_{j+1}} \frac{\partial \underline{\delta}_{j+1}}{\partial \underline{x}_{i+j-2}}.$$

The two components above are computed in the same fashion, and we now only demonstrate the derivation for $\underline{\Omega}_j$. The first term in $\underline{\Omega}_j$ can be obtained via the recursion in (10) according to the following derivation¹

$$\frac{\partial \underline{\omega}}{\partial \underline{\omega}_j} = \frac{\partial \underline{\omega}}{\partial \underline{\omega}_3} \prod_{k=1}^{3-j} \frac{\partial \underline{\omega}_{4-k}}{\partial \underline{\omega}_{3-k}} = \prod_{k=1}^{3-j} \mathcal{R}(\underline{e}_{4-k}^{-1}),$$

and the second term is derived as

$$\frac{\partial \underline{\omega}_j}{\partial \underline{\delta}_j} = \lambda_j \frac{\partial (\mathcal{R}(\underline{r}) \underline{\omega}_{j-1})}{\partial \underline{r}} \bigg|_{\underline{r}=\underline{e}_j^{-1}} \mathbf{D} \frac{\partial \text{Exp}_\perp(\underline{v})}{\partial \underline{v}} \bigg|_{\underline{v}=\lambda_j \underline{\delta}_j} + 2\lambda_j \mathbf{I}_3.$$

$\partial(\mathcal{R}(\underline{r}) \underline{\omega}_{j-1})/\partial \underline{r}$ denotes the Jacobian of quaternion rotation that is given by (174) in [10]. And the last term $\partial \underline{\delta}_j/\partial \underline{x}_{i+j-2}$ is available in (12).

Jacobian of acceleration interpolation: We again apply the general formulation in (11) to the acceleration interpolation in (4). It is then straightforward to obtain the desired Jacobian with the following expression

$$\frac{d\underline{\ddot{s}}}{d\underline{\delta}_{i+j-2}} = (\mathbb{I}_{j \neq 0}\ddot{\lambda}_j - \mathbb{I}_{j \neq 3}\ddot{\lambda}_{j+1})\mathbf{I}_3.$$

IV. ONLINE UWB-INERTIAL SPLINE FUSION

A. Sliding-Window Spline Fitting

Shown in Fig. 3, we exploit cubic B-splines to parameterize state (1) continuously over time with control points concatenated as $\underline{x} = [\underline{x}^\top, \underline{\dot{x}}^\top, \underline{\ddot{x}}^\top]^\top \in \mathbb{R}^{13}$. To keep the computational intensity tractable for online performance, we bound the spline fitting problem over a window of recent τ_w control points $\mathcal{X}_w = [\underline{x}_1, \dots, \underline{x}_{\tau_w}] \in \mathbb{R}^{13 \times \tau_w}$, namely,

$$\mathcal{X}_w^* = \arg \min_{\mathcal{X}_w} \mathcal{F}(\mathcal{X}_w), \quad (14)$$

with the objective function formulated as $\mathcal{F}(\mathcal{X}_w) =$

$$\nu_u \sum_{i=1}^m \|\mathcal{E}_u(\mathcal{X}_w, \hat{z}_{u,i})\|_{\mathbf{C}_u}^2 + \nu_i \sum_{k=1}^n \|\mathcal{E}_i(\mathcal{X}_w, \hat{z}_{i,k})\|_{\mathbf{C}_i}^2. \quad (15)$$

¹For cubic cumulative B-spline, we have $\underline{\omega}(t) = \underline{\omega}_k(t)$ with $k = 3$.

\mathcal{E}_u and \mathcal{E}_i denote residual terms built upon UWB and IMU measurements, $\{\hat{z}_{u,i}\}_{i=1}^m$ and $\{\hat{z}_{i,k}\}_{k=1}^n$, respectively, each observed at raw timestamps. \mathbf{C}_o and ν_o are covariance matrices and weights for each error term (Subscript 'o' stands for 'u' or 'i' for UWB or IMU sensors, respectively). As the optimization window slides, the so-called *active* control points within current window are updated over time until to be dropped out. Meanwhile, the three control points that are most recently removed from the window are turned into an *idle* state. They are no longer being optimized, however, still participate in computing residuals in current window via kinematic interpolations, which enables motion continuation across sliding windows over time. Note that timestamps of residuals and underlying control points are not to be aligned. This allows for flexible multi-sensor fusion and efficient state representation compared with discrete-time paradigm.

We now specify the residual terms in (15). Throughout the following derivations, all kinematic interpolations are associated with the IMU body (\mathcal{I}) and expressed w.r.t. world frame (\mathcal{W}). Anchor positions are given w.r.t. UWB frame (\mathcal{U}) with a transformation $\mathbf{T}_w^u \in \text{SE}(3)$ from world frame.

UWB residual: We demonstrate the UWB residual in (15) for time-of-arrival (ToA) ranging. Given a range measurement $\hat{z}_{u,i}$ at timestamp t_i , its residual term follows

$$\mathcal{E}_u(\mathbf{X}_w, \hat{z}_{u,i}) = \|\mathbf{T}_w^u \underline{s}_{ta,i}^w - \underline{a}_{an,i}^u\| - \hat{z}_{u,i}, \quad (16)$$

with $\underline{s}_{ta,i}^w = \underline{r}(t_i) \otimes \underline{\nu}_{ta}^T \otimes \underline{r}^{-1}(t_i) + \underline{s}(t_i)$ being the UWB tag position in world frame obtained by transforming tag coordinates $\underline{\nu}_{ta}^T$ w.r.t. body pose interpolated at t_i . $\underline{a}_{an,i}^u$ denotes coordinates of the corresponding anchor. Residual for time-difference-of-arrival (TDoA) ranging can be obtained similarly, which we do not specify due to page limit.

IMU residual: Given the k -th IMU reading $\hat{z}_{i,k}$ of acceleration $\hat{\underline{a}}_k^T$ and angular velocity $\hat{\underline{\omega}}_k^T$, we construct residual

$$\mathcal{E}_i(\mathbf{X}_w, \hat{z}_{i,k}) = [\underline{z}_{acc,k}^T, \underline{z}_{gyro,k}^T, \underline{z}_{bias,k}^T]^T$$

for spline fitting to inertial data. The accelerometer residual $\underline{z}_{acc,k}$ is given by

$$\underline{z}_{acc,k} = \underline{a}_k^T + \underline{b}_{acc,k} - \hat{\underline{a}}_k^T, \quad (17)$$

with $\underline{a}_k^T = \underline{r}^{-1}(t_k) \otimes (\ddot{\underline{s}}(t_k) + \underline{g}^w) \otimes \underline{r}(t_k)$ transforming the interpolated acceleration $\ddot{\underline{s}}(t_k)$ together with gravity \underline{g}^w to body frame. $\underline{b}_{acc,k}$ is the accelerometer bias interpolated on spline $\underline{b}(t)$ at t_k . The gyroscope residual $\underline{z}_{gyro,k}$ follows

$$\underline{z}_{gyro,k} = \underline{\omega}^T(t_k) + \underline{b}_{gyro,k} - \hat{\underline{\omega}}_k^T,$$

with $\underline{\omega}^T(t_k)$ interpolated recursively as shown in (10). $\underline{b}_{gyro,k}$ denotes the gyroscope bias interpolated at t_k . Further, we compute the difference of consecutive bias interpolations at t_k and t_{k+1} to obtain IMU bias residual

$$\underline{z}_{bias,k} = \underline{b}(t_{k+1}) - \underline{b}(t_k).$$

B. Concurrent Calibration

In general, transformation \mathbf{T}_w^u from world to UWB frames in (16) is unknown and is typically dependent on the anchor coordinates and initial tag pose at system initialization. Also,

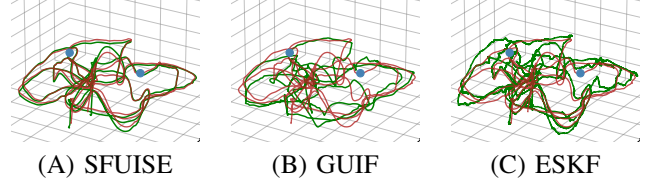


Fig. 4: Qualitative comparison on n4-i7-o2-n1.

the gravity orientation \underline{g}^w (obtained via normalizing the gravity $\underline{g}^w = \|\underline{g}^w\| \underline{g}^w$) in (17) is in general not available upon navigation. For approximating it, a common practice is to average the first several accelerometer readings under the assumption of a static motion start from a horizon plane. However, this can be easily violated by an undesired starting condition (e.g., on the fly). To address these issues, we estimate the frame transformation \mathbf{T}_w^u and the gravity orientation \underline{g}^w together with control points via spline fitting during the window-growing phase (illustrated in Fig. 2).

V. EVALUATION

A. Implementation and Evaluation Setup

The proposed spline fusion-based ultra-wideband-inertial state estimation (SFUISE) scheme is developed in C++ using ROS [30]. The system composes two individual nodes corresponding to the two functional blocks in the system pipeline Fig. 2. We implement a customized Levenberg-Marquardt (LM) algorithm for solving the nonlinear least squares in spline fitting, and both ToA and TDoA ranging principles of UWB are supported. Besides basic computational tools such as Eigen², no further external dependency is required.

The proposed system is evaluated in real-world scenarios based on the public data set UTIL [31] and own experiments, incorporating both ToA and TDoA ultra-wideband data. Two major discrete-time sensor fusion schemes from state of the art are considered for comparison. An own composition of graph-based UWB-inertial fusion (GUIF) system is developed with reference to [32] and [2]. Here, discrete-time states are estimated via sliding window optimization with residuals of IMU preintegration, UWB ranging and the prior factor from marginalization. Online calibration of \mathbf{T}_w^u is enabled during window-growing stage. Further, we deploy the error-state Kalman filter (ESKF) provided by [31] for evaluation against the recursive estimation scheme. In order to achieve functional UWB ranging under signal interference, the three systems are equipped with a simple thresholding step to reject outliers in UWB measurements.

Throughout the evaluation, SFUISE is configured with a sliding window of 100 control points at 10 Hz. All UWB readings are exploited for state estimation without down-sampling. In order to devote the focus to investigating the core sensor fusion scheme, we avoid fine-tuning of system configuration parameters.

²<https://eigen.tuxfamily.org>

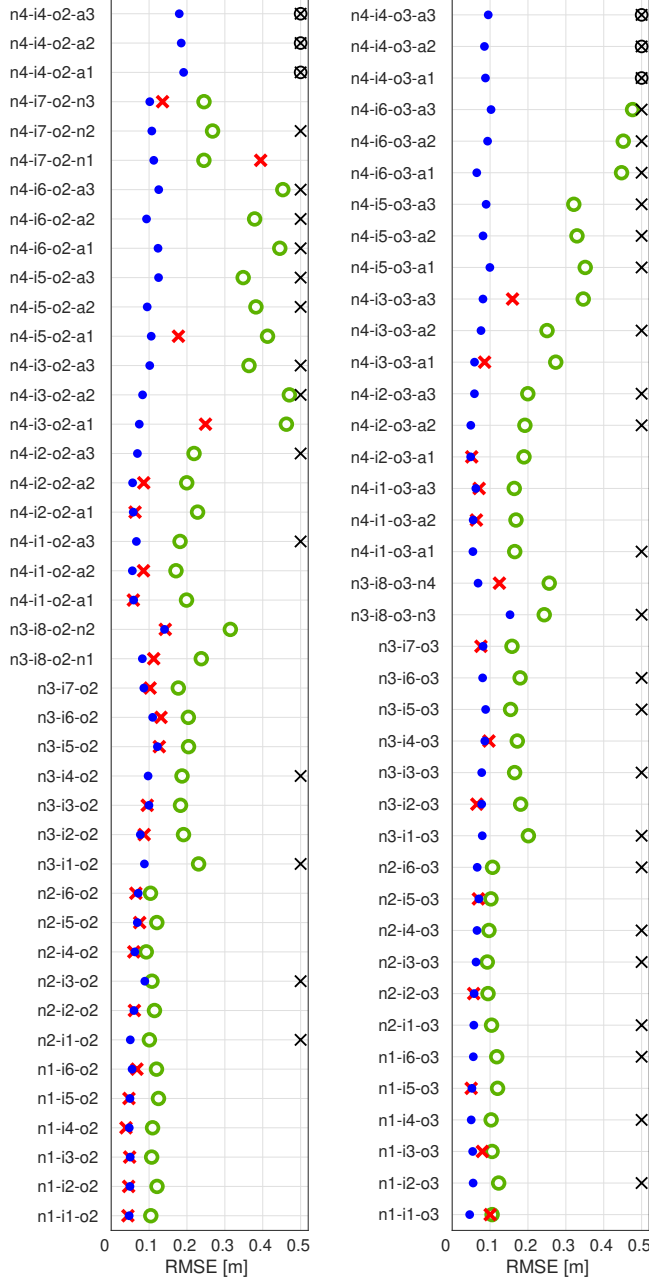


Fig. 5: APE (RMSE) in meters from evaluation on UTIL data set. Results from SFUISE are plotted with \bullet . Results from ESKF and GUIF are given by \circ and \times indicating tracking fails, respectively.

B. Public Data Set

We exploit UTIL flight data set for evaluating the proposed UWB-inertial fusion scheme with TDoA ultra-wideband ranging. Overall 81 sequences are collected on-board a quadcopter mounted with a UWB tag and an IMU (1000 Hz). The UWB sensor network is low-cost and operated at both centralized (tdoa2) and decentralized (tdoa3) modes under four different anchor constellations (const1-4). The TDoA measurements are collected with data rates ranging from 200 to 500 Hz including numerous

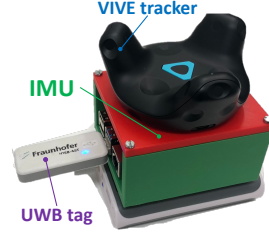


Fig. 6: Miniature sensor suite for recording ISAS-Walk.

challenging scenarios created by static and dynamic obstacles of various types of materials. Given control point estimates from SFUISE, we obtain the global pose trajectory via interpolation at the frame rate of ground truth (200 Hz), w.r.t. which we compute the RMSE of the absolute position error (APE) to quantify tracking accuracy.

As shown in Fig.5, results given by the three systems are summarized for each UWB operation mode. For brevity, we rewrite sequence names by taking the third letter of each word after de-hyphenation (e.g., sequence `const1-trial1-tdoa2` is shortened as `n1-i1-o2`). The proposed spline fusion scheme delivers superior performance over discrete-time approaches using recursive estimation or graph-based optimization. In particular, it exhibits a fairly good robustness against challenging conditions, e.g., in sequences with `const4` (`n4` in plot), where the tracking space is cluttered with static and dynamic obstacles of different materials including metal. In face of time-varying NLOS and multi-path interference, discrete-time approaches are more easily affected, delivering large tracking errors or even total fails. For demonstration, we plot results of a few representative runs of SFUISE in Fig.1. Another qualitative comparison of spline fusion with discrete-time schemes is shown in Fig.4 based on sequence `const4-trial7-tdoa2-manual1` (shortened as `n4-i7-o2-n1`). In all plots, green and red curves indicate estimates and ground truth, respectively.

Runtime: As shown in Fig.2, the two functional modules in the system pipeline run in parallel, and the spline fusion module dominates computational cost compared with the lightweight estimation interface. We conduct the mass evaluation on UTIL using a desktop (Intel Xeon E5-1620 CPU, 32 GB RAM) and record runtime of the backend fusion module w.r.t. the frame rate of control points. The proposed system delivers real-time performance with average runtime of 68.0 ± 3.1 ms and 58.5 ± 3.4 ms throughout subsets `tdoa2` and `tdoa3`, respectively. The small standard deviations indicate a well-bounded computational cost during sliding-window spline fusion. According to our investigation, solving the nonlinear least squares in (15) using the customized LM method usually converges within five iterations.

C. Experiment

To further evaluate the proposed scheme on UWB-inertial fusion using ToA ranging, a miniature sensor suite has been

TABLE I: APE (RMSE) in meters on ISAS-Walk.

Sequence	SFUISE	GUIF	ESKF
Walk1	0.117	0.143	0.225
Walk2	0.094	0.098	0.245
Walk3	0.094	0.229	0.270

instrumented as shown in Fig. 6. It is composed of a UWB tag provided by Fraunhofer IOSB-AST and an IMU embedded on Sense HAT (B), both mounted to a Raspberry Pi for sensor coordination and data recording³. An additional VIVE tracker is added to provide ground truth⁴. Overall three sequences, ISAS-Walk1, ISAS-Walk2 and ISAS-Walk3, are recorded during indoor walks with inertial and ultra-wideband (including five anchors) readings both at a frame rate of about 80 Hz. We list the APE in RMSE (m) given by the three systems in Tab. I. The proposed scheme SFUISE produces the best tracking accuracy consistently throughout the data set.

D. Discussion

As verified in the mass evaluation based on UTIL and ISAS-Walk, SFUISE shows superior performance over discrete-time fusion schemes, particularly, in unfavorable scenarios of signal interference and complex noise patterns that are hard or infeasible to detect and model. Since any kinematic interpolation refers to four consecutive control points (for cubic B-splines), the induced pose trajectory inherently guarantees motion continuation up to the second order. In comparison with discrete-time fusions, this implicitly brings extra constraints to solving the nonlinear optimization problem in spline fitting, while still acknowledging the locality of observations. As a result, sensor fusion exhibits better stability and robustness under challenging conditions even together with online calibration.

To further highlight the strength of spline fusion in UWB-based tracking, we exploit const1-trial1-tdoa2 (abbreviated as n1-i1-o2) from UTIL and discard IMU readings for UWB-only tracking. We run SFUISE and GUIF at estimation frame rates of 1 Hz and 10 Hz, respectively, with sliding windows both configured as 10 seconds to guarantee same amount of TDoA measurements for online estimation. We demonstrate a qualitative comparison in Fig. 7 with ground truth plotted in red. Due to signal noise and interference, graph-based approach produces physically-infeasible motion estimates, whereas the proposed continuous-time scheme delivers much smoother trajectory with much more efficient state representation using control points (1/10 memory consumption of discrete-time states).

VI. CONCLUSION

In this work, we propose a new framework for continuous-time state estimation using ultra-wideband-inertial sensors. Quaternion-based cubic B-splines are exploited for six-DoF

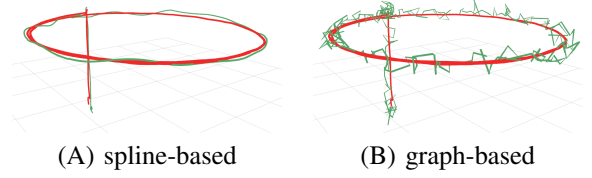


Fig. 7: UWB-only tracking on n1-i1-o2 of UTIL.

motion representation, based on which we systematically derive a complete set of theoretical tools for efficient spline fitting, including analytical kinematic interpolations and spatial differentiations on B-splines. This further facilitates the establishment of the novel sliding-window spline fusion scheme for online UWB-inertial state estimation. The resulted system, SFUISE, is evaluated in real-world scenarios based on public data set and experiments. It is real-time capable and shows superior performance over major discrete-time estimation approaches w.r.t. tracking accuracy, robustness and deployment flexibility.

There still remains considerable potential to exploit the proposed scheme. B-splines of nonuniform control points can be further investigated to achieve more efficient state representation and estimation [33]. Based on our theoretical contribution and open-source implementation, extensive engineering practice can be equipped with continuous-time paradigm in areas of automatic control, path planing, odometry and mapping [2], [13], [34], [35], etc.

APPENDIX

A. Jacobian of quaternion exponential map

For any point $\underline{v} \in \mathbb{R}^3$ in the tangent space at identity $\mathbb{1}$ on the manifold of unit quaternions, it can be retracted to \mathbb{S}^3 via exponential map according to $\text{Exp}_{\mathbb{1}}(\underline{v}) = [\cos \|\underline{v}\|, \underline{v}^\top \text{sinc} \|\underline{v}\|]^\top \in \mathbb{S}^3$, with $\|\cdot\|$ denoting the \mathcal{L}_2 norm [29]. Jacobian of exponential map is $\partial \text{Exp}_{\mathbb{1}}(\underline{v}) / \partial \underline{v} = [(\partial(\cos \|\underline{v}\|) / \partial \underline{v})^\top, (\partial(\underline{v} \text{sinc} \|\underline{v}\|) / \partial \underline{v})^\top]^\top \in \mathbb{R}^{4 \times 3}$, with the two items expressed as $\partial(\cos \|\underline{v}\|) / \partial \underline{v} = -\underline{v}^\top \text{sinc} \|\underline{v}\|$ and $\partial(\underline{v} \text{sinc} \|\underline{v}\|) / \partial \underline{v} = \frac{\cos \|\underline{v}\| - \text{sinc} \|\underline{v}\|}{\|\underline{v}\|^2} \underline{v} \underline{v}^\top + \mathbf{I}_3 \text{sinc} \|\underline{v}\|$.

B. Jacobian of quaternion logarithm map

Given any unit quaternion $\underline{r} = [r_0, \underline{r}_v^\top]^\top \in \mathbb{S}^3$ with r_0 and \underline{r}_v denoting the scalar and vector components, the rotation angle and axis can be retrieved by definition as $\theta = 2 \arctan(\|\underline{r}_v\| / r_0)$ and $\underline{u} = \underline{r}_v / \|\underline{r}_v\|$, respectively. It can be mapped to the tangent space at $\mathbb{1}$ via logarithm map

$$\text{Log}_{\mathbb{1}}(\underline{r}) = \theta / 2 \cdot \underline{u} = \arctan(\|\underline{r}_v\| / r_0) \underline{r}_v / \|\underline{r}_v\| \in \mathbb{R}^3. \quad (18)$$

The Jacobian of logarithm map follows $\partial \text{Log}_{\mathbb{1}}(\underline{r}) / \partial \underline{r} = [\partial \text{Log}_{\mathbb{1}}(\underline{r}) / \partial r_0, \partial \text{Log}_{\mathbb{1}}(\underline{r}) / \partial \underline{r}_v] \in \mathbb{R}^{3 \times 4}$, with the components given by $\partial \text{Log}_{\mathbb{1}}(\underline{r}) / \partial r_0 = -\underline{r}_v$ and $\partial \text{Log}_{\mathbb{1}}(\underline{r}) / \partial \underline{r}_v = \frac{1}{\|\underline{r}_v\|^2} (r_0 \underline{r}_v \underline{r}_v^\top + \frac{\|\underline{r}_v\|^2 \mathbf{I}_3 - \underline{r}_v \underline{r}_v^\top}{\|\underline{r}_v\|} \arctan \frac{\|\underline{r}_v\|}{r_0})$.

ACKNOWLEDGMENT

We would like to thank Norbert Fränzel from Fraunhofer IOSB-AST and Christopher Funk for help with instrumenting the sensor suite to record ISAS-Walk data set.

³<https://www.waveshare.com>

⁴<https://www.vive.com>

REFERENCES

- [1] A. Geiger, P. Lenz, C. Stiller, and R. Urtasun, "Vision Meets Robotics: The KITTI Dataset," *The International Journal of Robotics Research*, vol. 32, no. 11, pp. 1231–1237, 2013.
- [2] K. Li, M. Li, and U. D. Hanebeck, "Towards High-Performance Solid-State-LiDAR-Inertial Odometry and Mapping," *IEEE Robotics and Automation Letters*, vol. 6, no. 3, pp. 5167–5174, 2021.
- [3] S. Leutenegger, S. Lynen, M. Bosse, R. Siegwart, and P. Furgale, "Keyframe-Based Visual-Inertial Odometry Using Nonlinear Optimization," *The International Journal of Robotics Research*, vol. 34, no. 3, pp. 314–334, 2015.
- [4] H. Möls, K. Li, and U. D. Hanebeck, "Highly Parallelizable Plane Extraction for Organized Point Clouds Using Spherical Convex Hulls," in *2020 IEEE International Conference on Robotics and Automation (ICRA 2020)*, Paris, France, May 2020.
- [5] M.-G. Li, H. Zhu, S.-Z. You, and C.-Q. Tang, "UWB-Based Localization System Aided With Inertial Sensor for Underground Coal Mine Applications," *IEEE Sensors Journal*, vol. 20, no. 12, pp. 6652–6669, 2020.
- [6] S. Zheng, Z. Li, Y. Liu, H. Zhang, and X. Zou, "An Optimization-Based UWB-IMU Fusion Framework for UGV," *IEEE Sensors Journal*, vol. 22, no. 5, pp. 4369–4377, 2022.
- [7] J. D. Hol, F. Dijkstra, H. Luinge, and T. B. Schon, "Tightly Coupled UWB/IMU Pose Estimation," in *2009 IEEE International Conference on Ultra-Wideband*, Vancouver, BC, Canada, Sep. 2009.
- [8] M. Kok, J. D. Hol, and T. B. Schön, "Indoor Positioning Using Ultrawideband and Inertial Measurements," *IEEE Transactions on Vehicular Technology*, vol. 64, no. 4, pp. 1293–1303, 2015.
- [9] J. Li, Y. Bi, K. Li, K. Wang, F. Lin, and B. M. Chen, "Accurate 3D Localization for MAV Swarms by UWB and IMU Fusion," in *2018 IEEE International Conference on Control and Automation (ICCA)*, 2018, pp. 100–105.
- [10] J. Sola, "Quaternion Kinematics for the Error-State Kalman Filter," *arXiv preprint arXiv:1711.02508*, 2017.
- [11] A. Goudar and A. P. Schoellig, "Online Spatio-temporal Calibration of Tightly-coupled Ultrawideband-aided Inertial Localization," in *2021 IEEE/RSJ International Conference on Intelligent Robots and Systems (IROS)*, 2021.
- [12] H. Strasdat, J. M. M. Montiel, and A. J. Davison, "Real-Time Monocular SLAM: Why Filter?" in *2010 IEEE International Conference on Robotics and Automation (ICRA)*, Anchorage, AK, USA, May 2010.
- [13] T. Qin, P. Li, and S. Shen, "VINS-Mono: A Robust and Versatile Monocular Visual-Inertial State Estimator," *IEEE Transactions on Robotics*, vol. 34, no. 4, pp. 1004–1020, 2018.
- [14] A. Reinke, M. Palieri, B. Morrell, Y. Chang, K. Ebadi, L. Carlone, and A.-A. Agha-Mohammadi, "LOCUS 2.0: Robust and Computationally Efficient Lidar Odometry for Real-Time 3D Mapping," *IEEE Robotics and Automation Letters*, vol. 7, no. 4, pp. 9043–9050, 2022.
- [15] Y. Song and L.-T. Hsu, "Tightly Coupled Integrated Navigation System via Factor Graph for UAV Indoor Localization," *Aerospace Science and Technology*, vol. 108, p. 106370, 2021.
- [16] P. Furgale, T. D. Barfoot, and G. Sibley, "Continuous-Time Batch Estimation Using Temporal Basis Functions," in *2012 IEEE International Conference on Robotics and Automation (ICRA)*, Saint Paul, MN, USA, May 2012.
- [17] S. Anderson and T. D. Barfoot, "Towards Relative Continuous-Time SLAM," in *2013 IEEE International Conference on Robotics and Automation (ICRA)*, Karlsruhe, Germany, May 2013.
- [18] H. Sommer, J. R. Forbes, R. Siegwart, and P. Furgale, "Continuous-Time Estimation of Attitude Using B-Splines on Lie Groups," *Journal of Guidance, Control, and Dynamics*, vol. 39, no. 2, pp. 242–261, 2016.
- [19] P. Furgale, J. Rehder, and R. Siegwart, "Unified Temporal and Spatial Calibration for Multi-sensor Systems," in *2013 IEEE/RSJ International Conference on Intelligent Robots and Systems (IROS)*, Tokyo, Japan, Nov. 2013.
- [20] A. Patron-Perez, S. Lovegrove, and G. Sibley, "A Spline-Based Trajectory Representation for Sensor Fusion and Rolling Shutter Cameras," *International Journal of Computer Vision*, vol. 113, no. 3, pp. 208–219, 2015.
- [21] E. Mueggler, G. Gallego, H. Rebecq, and D. Scaramuzza, "Continuous-Time Visual-Inertial Odometry for Event Cameras," *IEEE Transactions on Robotics*, vol. 34, no. 6, pp. 1425–1440, 2018.
- [22] J. Lv, K. Hu, J. Xu, Y. Liu, X. Ma, and X. Zuo, "CLINS: Continuous-Time Trajectory Estimation for LiDAR-Inertial System," in *2021 IEEE/RSJ International Conference on Intelligent Robots and Systems (IROS)*. IEEE, 2021, pp. 6657–6663.
- [23] G. Cioffi, T. Cieslewski, and D. Scaramuzza, "Continuous-Time Vs. Discrete-Time Vision-Based SLAM: A Comparative Study," *IEEE Robotics and Automation Letters*, vol. 7, no. 2, pp. 2399–2406, 2022.
- [24] C. Sommer, V. Usenko, D. Schubert, N. Demmel, and D. Cremers, "Efficient Derivative Computation for Cumulative B-Splines on Lie Groups," in *Proceedings of the IEEE/CVF Conference on Computer Vision and Pattern Recognition (CVPR)*, Seattle, WA, USA, June 2020.
- [25] J. Tirado and J. Civera, "Jacobian Computation for Cumulative B-Splines on SE(3) and Application to Continuous-Time Object Tracking," *IEEE Robotics and Automation Letters*, vol. 7, no. 3, pp. 7132–7139, 2022.
- [26] A. J. Yang, C. Cui, I. A. Bârsan, R. Urtasun, and S. Wang, "Asynchronous Multi-View SLAM," in *2021 IEEE International Conference on Robotics and Automation (ICRA)*, Xi'an, China, May 2021.
- [27] D. Hug, P. Banninger, I. Alzugaray, and M. Chli, "Continuous-Time Stereo-Inertial Odometry," *IEEE Robotics and Automation Letters*, vol. 7, no. 3, pp. 6455–6462, 2022.
- [28] M. Persson, G. Häger, H. Övrén, and P.-E. Forssén, "Practical Pose Trajectory Splines With Explicit Regularization," in *2021 International Conference on 3D Vision (3DV)*. IEEE, 2021, pp. 156–165.
- [29] K. Li, "On-Manifold Recursive Bayesian Estimation for Directional Domains," Ph.D. dissertation, Karlsruher Institut of Technology (KIT), 2022.
- [30] M. Quigley, B. Gerkey, K. Conley, J. Faust, T. Foote, J. Leibs, E. Berger, R. Wheeler, and A. Ng, "ROS: An Open-source Robot Operating System," *ICRA Workshop on Open Source Software*, vol. 3, no. 3.2, p. 5, 2009.
- [31] W. Zhao, A. Goudar, X. Qiao, and A. P. Schoellig, "UTIL: An Ultra-Wideband Time-Difference-of-Arrival Indoor Localization Dataset," *arXiv preprint arXiv:2203.14471*, 2022.
- [32] G. Cioffi and D. Scaramuzza, "Tightly-coupled Fusion of Global Positional Measurements in Optimization-based Visual-Inertial Odometry," in *2020 IEEE/RSJ International Conference on Intelligent Robots and Systems (IROS)*, Las Vegas, NV, USA, Oct. 2020.
- [33] K. Qin, "General Matrix Representations for B-Splines," in *Proceedings Pacific Graphics' 98. Sixth Pacific Conference on Computer Graphics and Applications (Cat. No. 98EX208)*. IEEE, 1998, pp. 37–43.
- [34] M. Mukadam, X. Yan, and B. Boots, "Gaussian Process Motion planning," in *2016 IEEE International Conference on Robotics and Automation (ICRA)*, Stockholm, Sweden, May 2016.
- [35] N. Lv, J. Liu, and Y. Jia, "Dynamic Modeling and Control of Deformable Linear Objects for Single-Arm and Dual-Arm Robot Manipulations," *IEEE Transactions on Robotics*, vol. 38, no. 4, pp. 2341–2353, 2022.